Article

Multi-Platform Integrated Analysis of the Degradation Patterns of Impact Crater Populations on the Lunar Surface

Meixi Chen [1], Xinyu Ma [1], Teng Hu [1,2,*], Zhizhong Kang [1,2] and Meng Xiao [1]

1   School of Land Science and Technology, China University of Geosciences, Beijing 100083, China;
     1012214109@email.cugb.edu.cn (M.C.); 1012214108@email.cugb.edu.cn (X.M.); zzkang@cugb.edu.cn (Z.K.);
     2012210008@email.cugb.edu.cn (M.X.)
2   Subcenter of International Cooperation and Research on Lunar and Planetary Exploration, Center of Space
     Exploration, Ministry of Education of The People's Republic of China, Beijing 100083, China
*   Correspondence: huteng@cugb.edu.cn

Abstract: Following the processing of the Chang'e-4 satellite images, Chang'e-4 landing camera images, and Yutu-2 panoramic camera images, data were obtained in a variety of resolutions, including digital elevation model (DEM) and digital orthophoto map (DOM). By determining the morphological parameters, including the depths and diameters of impact craters in the study area, as well as their degradation classes based on surface texture features, we conducted a comprehensive analysis of the morphological parameters and population degradation patterns of impact craters from multiple platforms. The data from three platforms were employed to identify 12,089 impact craters with diameters ranging from 0.1 m to 800.0 m, which were then classified into five degradation classes based on their morphology in the images. This study indicates that as the size of impact craters increases, the population within them experiences a greater degree of degradation. However, the severe degradation of impact craters with diameters of less than 1 m or even 2 m is influenced by the rapid rate of degradation of the crater and the low solidity of the crater lips. The results of the equilibrium state of impact craters indicate that for sub-metre-sized impact craters (with diameters below 2.0 m), it is challenging to reach equilibrium. Furthermore, the smaller the impact crater, the more difficult it is to achieve equilibrium, which is probably the result of simpler generation conditions and the faster degradation of small impact craters.

Keywords: metre-to-centimetre-size impact craters; satellite images; landing camera images; Yutu-2 panoramic camera images; multi-angle analysis

1. Introduction

One of the most readily apparent features of the Moon's surface is the presence of impact craters [1]. The study of impact craters is of significant importance for the understanding of the lunar morphology, the rock structure of the Moon and the origin of the Moon [2–4]. The study of impact craters can be traced back to many years ago. In recent years, the scientific study of impact craters has been greatly facilitated by the ongoing lunar and deep space exploration missions [5]. A significant corpus of high-resolution remote sensing images of the lunar surface as well as other classes of scientific data have been and continue to be acquired, a large number of analyses of the morphological characteristics of impact craters have been conducted, and a database of impact craters of different sizes on the surfaces of Earth-like planets has been established [6]. Furthermore, researchers conducted an analysis of the impact crater populations, examining the degradation patterns of impact crater populations based on their degraded morphological features. The research is particularly concerned with the current production and degradation processes on the lunar surface, taking into account the characteristics of small young lunar impact craters [7]. This is significant for speculating the age of the geological units on the lunar surface as well as the evolution of the structure of the surface materials [8].

Previous studies of impact crater degradation were primarily based on images obtained from the lunar exploration satellites of the Chang'e project. The successful launch of Chang'e-4 has enabled the landing camera of the lander and the panoramic camera of the Yutu-2 rover to provide a substantial number of high-resolution images for in situ exploration and roving surveys of the lunar surface [9]. Consequently, the image data from disparate platforms enables the examination of the deterioration patterns of the impact crater populations from a multitude of vantages and in a comprehensive manner.

A substantial body of research has been conducted on the degradation patterns of impact craters. Currently, the method of impact craters' morphology–age relationship analysis is the principal research method employed by the majority of researchers. For instance, Craddock and Haruyama et al. investigated the process of impact crater degradation and proposed a method for determining the relative age of geological units based on the concept of a degradation parameter [10,11]; Wood, Ivanov et al. classified the degradation through the impact craters' morphology [12,13]; and Craddock established a degradation model and estimated the degradation and erosion rate of impact craters by using Clementine data [10]. The saturated equilibrium state of impact crater density has been studied; it is the state in which a crater population smaller than a given diameter is considered to be in equilibrium when the production rate of craters is balanced by the removal rate. For example, Hartman and James studied cratering equilibrium using computer modelling methods [14,15]. Cratering equilibrium is a crater population with a diameter smaller than a given diameter when the production rate of craters is balanced by the removal rate. Statistical studies of the morphology of degradation classes and other relevant features are crucial for elucidating the correlation between the morphological evolution of impact craters and the age of the corresponding lunar surface in the area. The classification of impact crater degradation has been predominantly based on visual interpretation. In 1963, Arthur proposed a classification of four degradation classes for the Moon. Class C1 comprises fresh impact craters, Class C2 initially degraded impact craters with smooth rims, Class C3 impact craters with severely eroded morphology, and Class C4 completely flattened impact craters. However, distinguishing the four degradation classes through visual interpretation may be much affected by subjective judgement and by crater size [16]. In 1976, five degradation classes were proposed for the Moon based on the study of McGill and Wise, Basilevsky et al. These comprised three main classes (A, B, and C) and two transitional classes (AB and BC) [17]. A refers to the fresh impact craters, Class B refers to the initially degraded impact craters (with smooth edges), and Class C refers to the completely flattened impact craters. The distinction between the five degradation classes may be significantly influenced by subjective judgement.

The current research on the degradation patterns of impact crater populations on the lunar surface is primarily conducted using the scientific data provided by the CCD stereo camera, which is equipped on the lunar exploration satellite; the scientific data provided by the landing camera, which is equipped on the lander; and the scientific data provided by the panoramic camera, which is equipped on the rover. In previous studies, satellite data were primarily employed to investigate kilometre- and sub-kilometre-sized impact craters on the lunar surface. Some researchers have demonstrated that the depth-to-diameter ratio of fresh simple craters on the Moon is approximately 0.2. Nevertheless, for fresh simple impact craters with a diameter of less than 1 km, the depth-to-diameter ratio is only 0.13, which may be related to the strength of the shallow lunar surface layer [18–21]. The database of Losiak et al. indicates that the depth-to-diameter ratio of impact craters with diameters between 1 m and 15 km is approximately 0.17 [22]. The observed low value of the ratio is likely the result of the degradation of some impact craters. The lunar frontal images captured by the Apollo 11 rover demonstrate the presence of a considerable number of fresh impact craters and severely degraded impact craters in the vicinity of the Apollo 11 landing site. Some researchers also compared the degradation patterns of impact craters on the Apollo 11 landing site with those in the Chang'e-4 landing area. Their findings indicated that the degradation of impact craters initially occurred at a rapid pace,

but the degradation rate subsequently decreased significantly as the degree of degradation increased [23].

In addition, the researchers who created the images from the rover also invested a great deal of effort into the project. Yang et al. employed the panoramic camera of the Yutu-2 rover to analyse the statistical pattern of secondary impact craters in the landing zone. The study demonstrated that the majority of impact craters exhibited a depth-to-diameter ratio within the range of 0.10 to 0.16. An analysis of the size–frequency distribution (SFD) of impact craters reveals that impact craters with diameters of tens of metres are typically in a saturated state, exhibiting a range of degradation patterns [24]. Hu et al. validated the degradation classes of impact craters by utilising the ground-based topographic camera and the panoramic camera on the Yutu-2, with a particular focus on analysing centimetre to metre impact craters, and assessed the equilibrium state of the centimetre to metre impact crater populations in the Chang'e-4 landing area. The conclusion was that more than 90% of the impact craters have moderately or severely degraded, and as with the degradation pattern of large impact crater populations, the smaller the size of the crater, the severer the degradation is. Moreover, Hu et al. demonstrated that it is more challenging to achieve equilibrium for small impact craters in 2022, with cumulative SFD slopes of -2.696 and -2.392 observed in these two areas. This may be attributed to the presence of secondary craters and/or resurfacing events resulting from ejecta from adjacent craters [25].

Existing studies generally agree that for impact craters of the same size, the earlier they were formed, i.e., the older they are, the more obvious their desegregation is, and the smaller the impact craters are, the likelier they are to disappear faster as a result of degradation. However, few studies have integrated satellite image data, landing camera image data, and rover image data for analysis. Consequently, in this study, we integrated three distinct datasets from disparate platforms with the objective of analysing the statistical degradation patterns of the impact crater populations from multiple platforms. This approach enabled us to achieve a comprehensive evaluation of the impact craters in the area, a feat that had not been accomplished in previous studies.

Section 2 mainly presents the experimental data and data processing methods employed in this paper. Section 3 presents the manual extraction results and classification results of impact craters from the data respectively from the satellite, landing camera, and rover. This includes a separate and comprehensive analysis of the outcomes from the three platforms. Section 4 compares the data from multiple perspectives and discusses the overall degradation and saturation status.

2. Data and Methodology

2.1. Methodology

This paper explores the distribution and degradation patterns of multi-platform impact craters by using downloaded image data from the satellite and the landing camera, as well as the processed image data from the panoramic camera. The image data include the digital elevation model (DEM) and the digital orthophoto map (DOM). Based on the image data, all of the recognizable impact craters in the images were manually extracted, and the degradation classification was carried out by taking into account the spatial morphologies of the impact craters. The specific process is shown in Figure 1. The detailed description of the method is as below.

2.2. Data and Processing

The image data are from Chang'e-4 satellite, Chang'e-4 landing camera, and Yutu-2 panoramic camera. Among them, the image data from Chang'e-4 satellite were downloaded from the SELENE (KAGUYA) dataset [26]. This DOM image's (M1298916428) resolution is 0.8 m. The data from Chang'e-4 landing camera were produced on the basis of the Chang'e-4 landing camera dataset. The ground resolution of the images was heterogeneous, the resolution of the landing camera increased from 0.09 m/pixel to 0.05 m/pixel when the camera descended along the main optical axis, and the georeferenced coordinates

(GCS_Moon_2000) were provided. The image data from the panoramic camera were produced on the basis of the Yutu-2 panoramic camera dataset, and the georeferenced coordinates (GCS_Moon_2000) were provided [27].
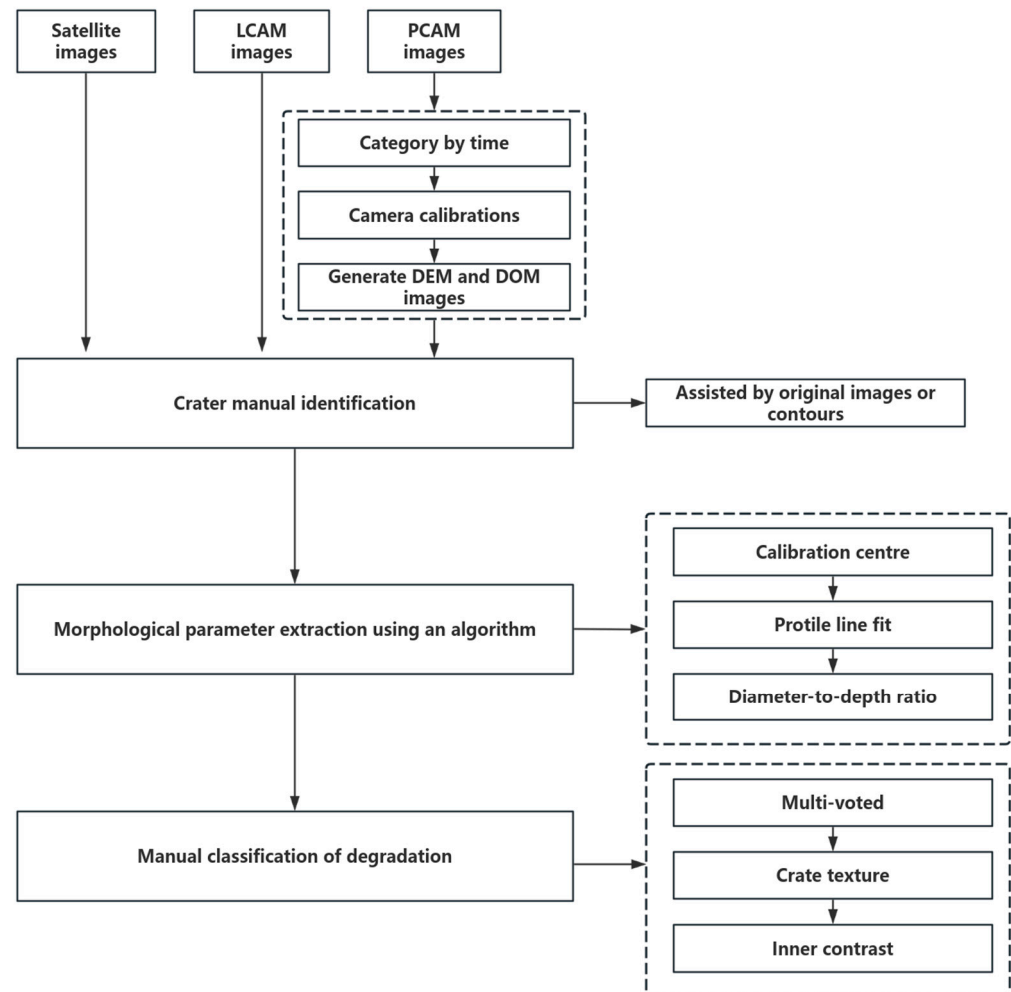

Figure 1. Flow chart of impact craters' data processing.

The panoramic camera has two modes—colour imaging and panchromatic imaging, which can be switched to each other during the shooting process. The image resolution of the colour mode is 2352×1728 pixels, while the image resolution of the panchromatic imaging mode is 1176×864 pixels, and the camera field-of-view angle is $19.6° \times 14.5°$ [9]. The panoramic camera relies on the up and down, left and right rotation of the mast to capture 360° images around the station, and 56 images can be captured in each turn, including 28 pairs of images in different directions at two altitude angles, thus realizing the three-dimensional stereo imaging of the topography and landscape of the landing area and the roving area [28]. By 20 September 2023, Chang'e-4 had completed its 62nd lunar day of work, and the data used in this paper are the images taken by the panoramic camera and produced from 1st to 40th lunar day.

The processing of images from the panoramic camera was divided into three steps. Firstly, the images were classified according to the time of production, and were divided into 66 stations, with each station including 122 image data files. The data from one station refers to the image data obtained from the Yutu-2 rover after it ceased forward motion, remained stationary, and was photographed by rotating the panoramic camera in the four cardinal directions. Images from each station were imported into MetashapePro1.7.4, where camera calibration and zooming were performed, and a dense point cloud was created. The focal length of the panchromatic camera is 50.29 mm, with the pixel being

0.0148 mm; the focal length of the colour camera is 50.274 mm, with the pixel being 0.0074 mm, and the zooming was based on the track width of Yutu-2—15 cm. Finally, through the dense point cloud, the grid image, the DEM image, and the DOM image were produced and the 3D model and corresponding texture were obtained at the same time. In particular, as the PCAM of Yutu-2 can achieve clear imaging at an infinite distance from the detector foot to the field of view, the DEM and DOM resolutions are variable, ranging from 0.0011–0.004 m/pixel.

2.3. Identification Methods

Impact craters are depressed and circular, so they can be identified through the contrast between light and dark under lighting conditions. In this paper, CraterTools [29] was used to identify and mark the impact craters in the generated DOM and DEM images.

In the identification process, we adopted a multi-source data fusion method, as shown in Figure 2. We manually identified the impact craters in the DOM and DEM images by identifying the depressed circles and the contrast of illuminated and shadowed areas. In the manual identification of impact craters, the approximate location of the impact crater is extracted, and it is not required to ensure that the identification results fit the centre and edges of the impact crater. The exact location of the impact crater and the extraction of morphological parameters were obtained based on an extraction algorithm, which results in improved extraction speed and accuracy. In addition, it is evident from Figure 2b,d,f that we created full-map contour lines on the basis of the DEM images to assist the identification of impact craters in the DOM images, where the interval between contour lines is 0.01 m. The purpose of creating contour lines is to better identify the complete morphology of the craters, and to more clearly find the impact craters that do not have obvious changes of depth in the DEM and DOM images. According to Figure 2a,b, image data from the satellite are mainly based on the impact craters identified through the DOM images and contour information established using DEM. As shown in Figure 2c,d, the data of impact craters from the landing camera (LCAM) were mainly identified by means of the 9 cm DOM images and the contour lines generated from the DEM images, similar to impact crater identification in satellite images. The identification of impact craters' images in the panoramic camera (PCAM) was more complicated. Due to the limitation of the imaging angle of the panoramic camera, the bottom of some impact craters failed to be photographed, so these incomplete images had to be abandoned. The metre-sized impact craters are small and shallow, without obvious contrast between illuminated and shadowed areas; as in Figure 2e,f, we used the contour based on the DEM images and DOM images generated to identify the impact craters, in which the elevation interval between contour lines is 0.01 m. As the completeness of the fit to the centre of the craters could not be clearly observed in the DOM images generated by the panoramic camera of the rover, when identifying these impact craters, we compared the DOM images with the original images taken by the rover to ensure the morphological completeness of such impact craters. Figure 2g illustrates the original images from the rover which correspond to Figure 2e.

2.4. Morphological Parameter Extraction

In this paper, an automatic extraction algorithm [30] involved the use of a technique designed to extract multi-morphological parameters from the impact craters, and the algorithm includes three steps, as shown in Figure 3. The algorithm firstly corrected the original data using the method of circle fitting, including the correction of the centroid offset and the position of the impact crater edge. The identification result of the offset is closer to the real position of the impact crater, so that the more accurate position and parameter information of the impact crater can be obtained and improve the data quality.

Subsequently, the least squares algorithm was employed to fit high-order polynomials to the profile lines of the impact crater. This resulted in the acquisition of high-order polynomial functions with a superior degree of fit, which were then used to obtain the fitted profile lines and the polynomial model. Finally, the morphology of the impact

crater profiles was described from a mathematical perspective. Finally, the automatic extraction algorithm, combined with the morphological method to analyse the impact crater profile, designed eight morphological descriptors, including single morphological parameters—depth, internal and external slope, pit lip width, pit lip height, etc.—and composite morphological parameters—roundness, depth-to-diameter ratio, and body shape ratio. The automatic extraction algorithm was designed to implement a range of extraction algorithms, each tailored to extract a specific morphological parameter. This paper primarily examines the morphological parameters, including impact crater diameter, depth, and depth-to-diameter ratio. These parameters offer insights into the shape, size, and evolution of impact craters.
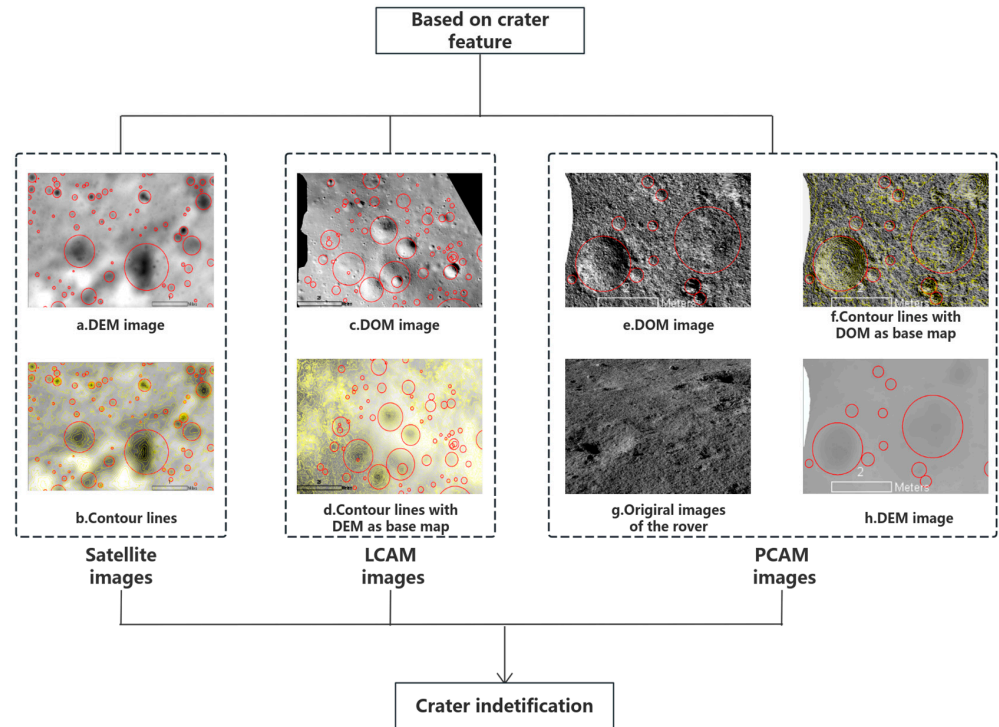
Figure 2. Impact crater identification method. The red outlined areas correspond to impact craters identified.
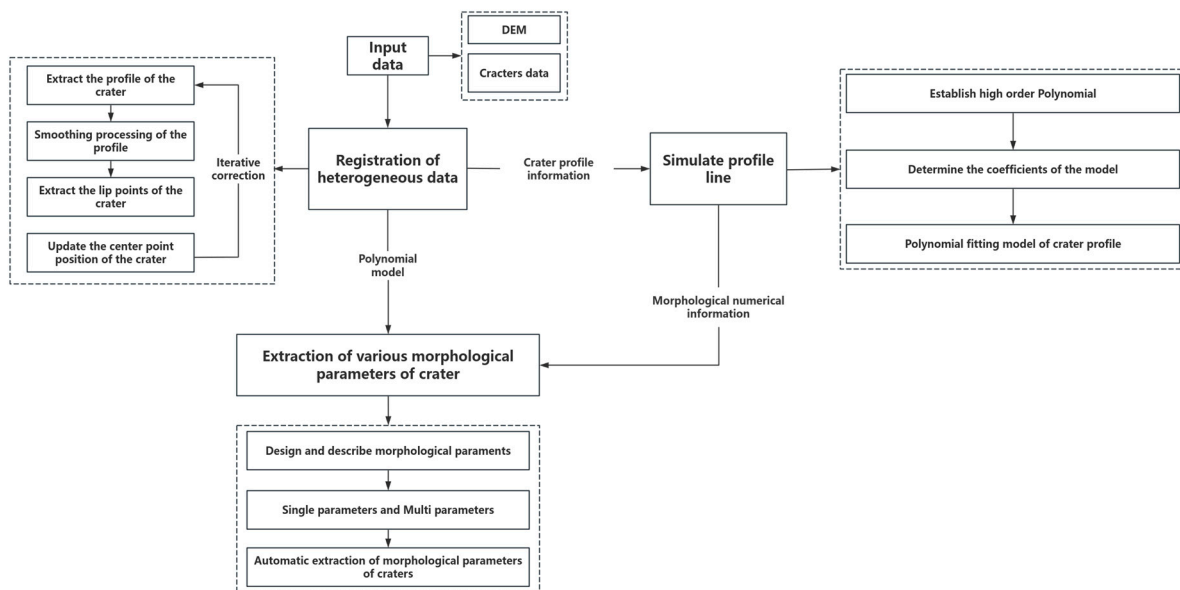
Figure 3. Crater morphological parameter extraction algorithm.

2.5. Degradation Classification

According to the study of Basilevsky et al. [17], impact craters were classified into five classes—A, AB, B, BC, and C—according to their different degrees of degradation. Among them, Class A refers to the freshest impact craters, and Class C refers to the mostly degraded impact craters. Table 1 illustrates examples of different types of impact craters on different platforms: Class A has obvious light or clear edges, deep crater, and sharp contrast between light and dark; Class AB has slight degradation with obvious contrast between light and dark; Class B has clear and intact edges, degradation traces, and obvious shadows; Class BC has incomplete edges, obvious degradation traces, and shallow craters with unobvious contrast between illuminated and shadowed areas; and Class C has blurred and incomplete edges, severe degradation, shallow crater, no shadows, and a circular outline that can be distinguished when the image is stretched. In addition, satellite image, LCAM image, and PCAM image were all taken on a lunar day with better illumination, which resulted in fewer impact crater shadows because of the lighting conditions and less impact on degradation classification.

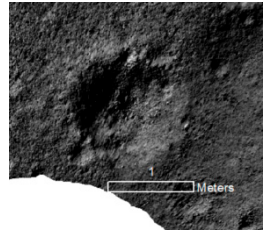**Table 1.** Examples of different classes of impact crater degradation from different platforms.
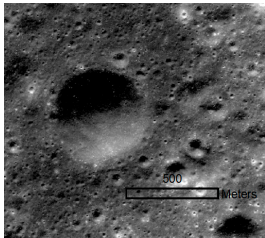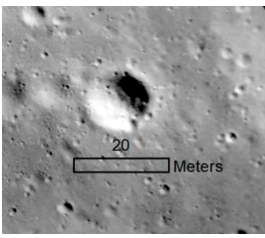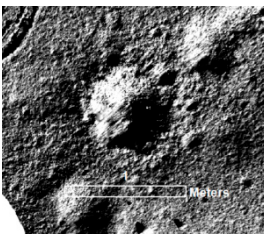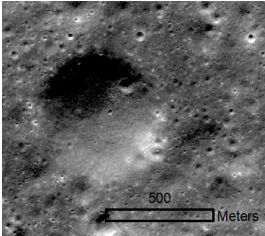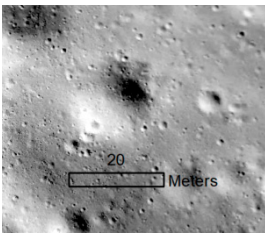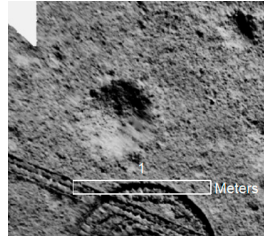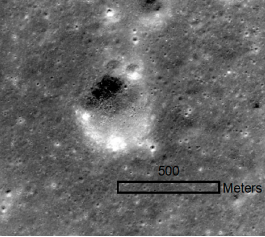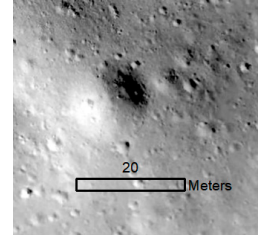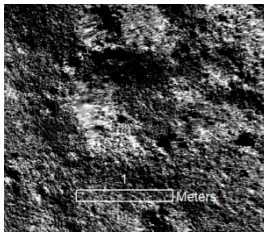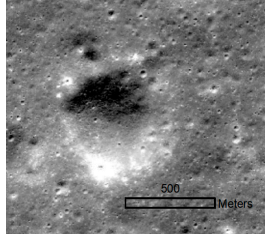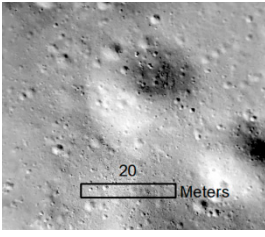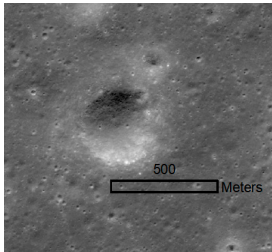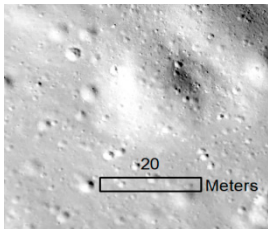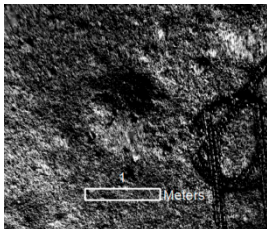
Classes	Satellite Images	LCAM Images	PCAM Images
A			
AB			
B			
BC			

Table 1. *Cont.*

Classes	Satellite Images	LCAM Images	PCAM Images
C			

In this paper, the degradation classes of impact craters were identified manually and qualitatively. Prior to the degradation classification, our researchers performed an overall identification of the impact craters in the different resolution images, for example, by judging the range of brightness and grey scale values of the images. The results of the overall identification are taken into account for impact crater classification, which reduces the impact of image resolution and solar elevation on the classification results. Manual and qualitative classification is usually affected by subjective factors, so judgement mistakes are inevitable. For instance, Class BC in Table 1 is analogous to Class C, which may result in misclassification. Consequently, a multiple voting procedure was applied to all impact craters. In the initial phase of the voting process, all impact craters were classified as degraded by three researchers. Subsequently, the degradation classes were collated. For any given impact crater, the degradation class would be confirmed only if the number of votes was 60% or more. In the event that the impact crater was not classified with a specific degradation class, it would be considered to have an uncertain degradation class and would require reclassification. Finally, all impact crater degradation classes received 60% or more support, thus allowing for the classification of the impact crater degradation to be completed.

3. Results

Based on the above research methods, we manually identified and extracted the impact craters' morphological parameters in the Chang'e-4 satellite image, Chang'e-4 LCAM image, and Yutu-2 PCAM images, and conducted statistics and analyses on their degradation degree. The completeness of the impact crater population statistics was mainly subject to the image resolution and illumination conditions, and the impact craters with a diameter longer than $10\times$ pixels had a higher confidence coefficient [31]. In order to provide a robust statistical analysis of crater degradation, it was deemed appropriate to consider 95% of the craters in the centre of each area to have a high confidence coefficient. All impact craters within the 95% confidence interval were subsequently presented in the results section. A total of 12,089 impact craters were manually extracted and located within the confidence interval. The minimum diameter of the impact crater identified in the panoramic camera image was 0.067m, the minimum diameter of the impact crater identified in the landing camera image was 1.55m, and the minimum diameter of the impact crater identified in the satellite imagery was 56.04 m, which are all greater than $10\times$ pixels.

3.1. Extraction

In order to extract the impact craters from the images captured by the Yutu-2 rover panoramic camera, we reconstructed the scenes of 66 stations and generated DEM images and DOM images, as illustrated in Figure 4. The results demonstrated the high image resolution and high completeness of the impact craters, which provided a robust foundation for the study of impact craters along the trajectory of the Yutu-2 rover.
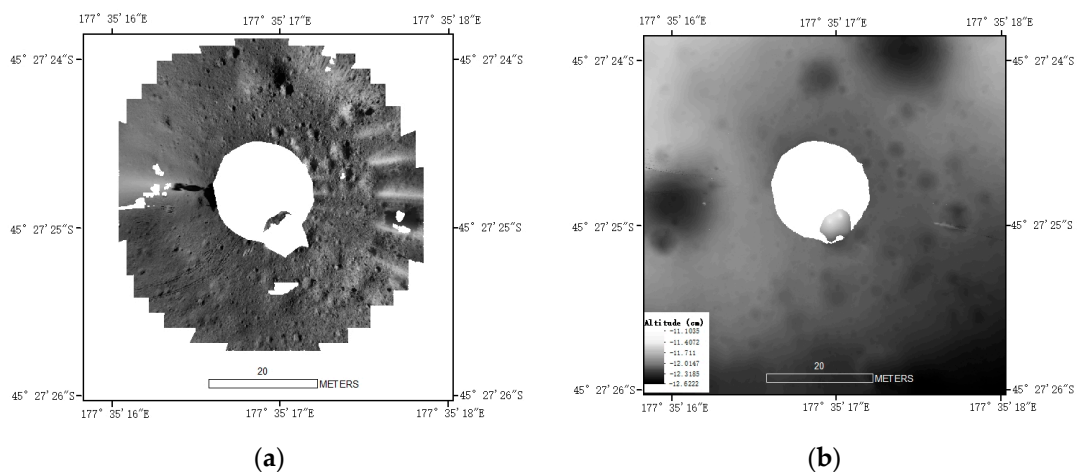
Figure 4. PCAM images. (**a**) DOM image. (**b**) DEM image.

The digital orthophotos of each station were employed as the fundamental study area, which was a circular area with an average outer diameter of 11 m and an inner diameter of 3 m, situated at the centre of the rover's position, with an average area of 297 m^2. Figure 5 illustrates the distribution of impact craters in the DOM image. It can be observed that there is a radial distribution around the rover, with the density of impact craters decreasing with increasing distance from the rover. A small number of complete impact craters can be seen to be scattered outside the DOM image. In general, the impact craters are numerous, relatively small in size, and distributed in close proximity to the centre of the rover. The distribution pattern of all impact craters extracted from all stations is essentially consistent with that shown in Figure 5.
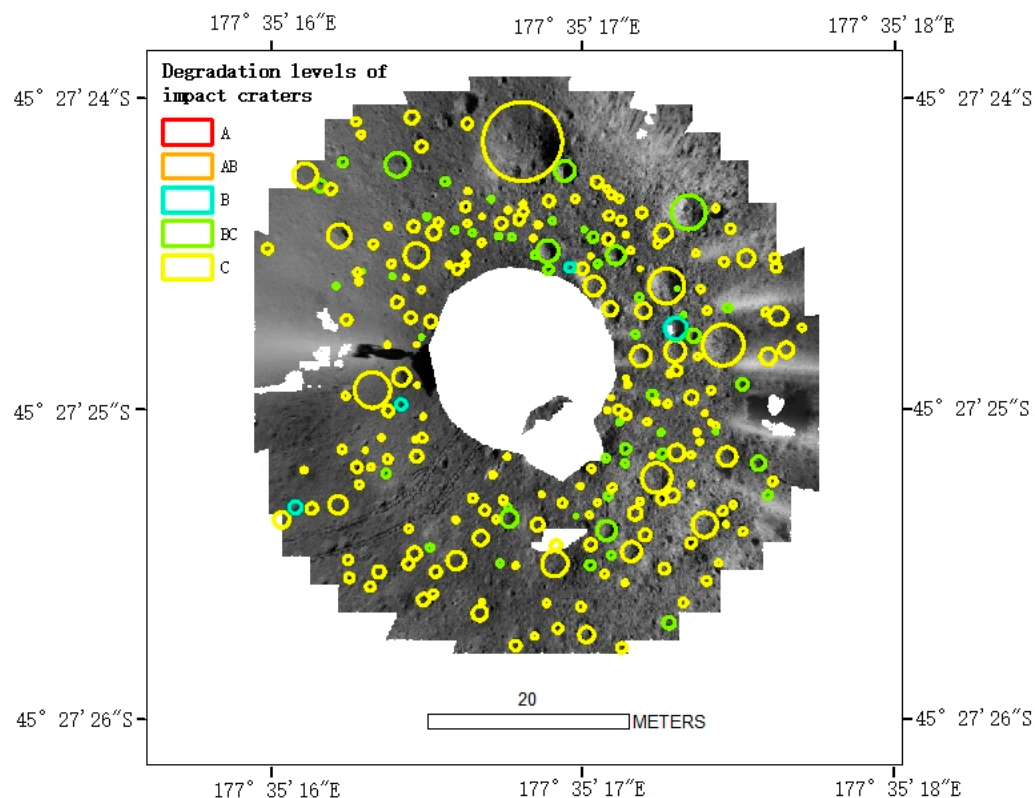

Figure 5. Identified impact craters in DOM images.

The extraction of the impact craters from the images captured by the landing camera of Chang'e-4 is illustrated in Figure 6. This figure also presents the image range and the extracted results. The total imaging area is 25,868 m², and the imaging range includes some images captured by the panoramic camera.
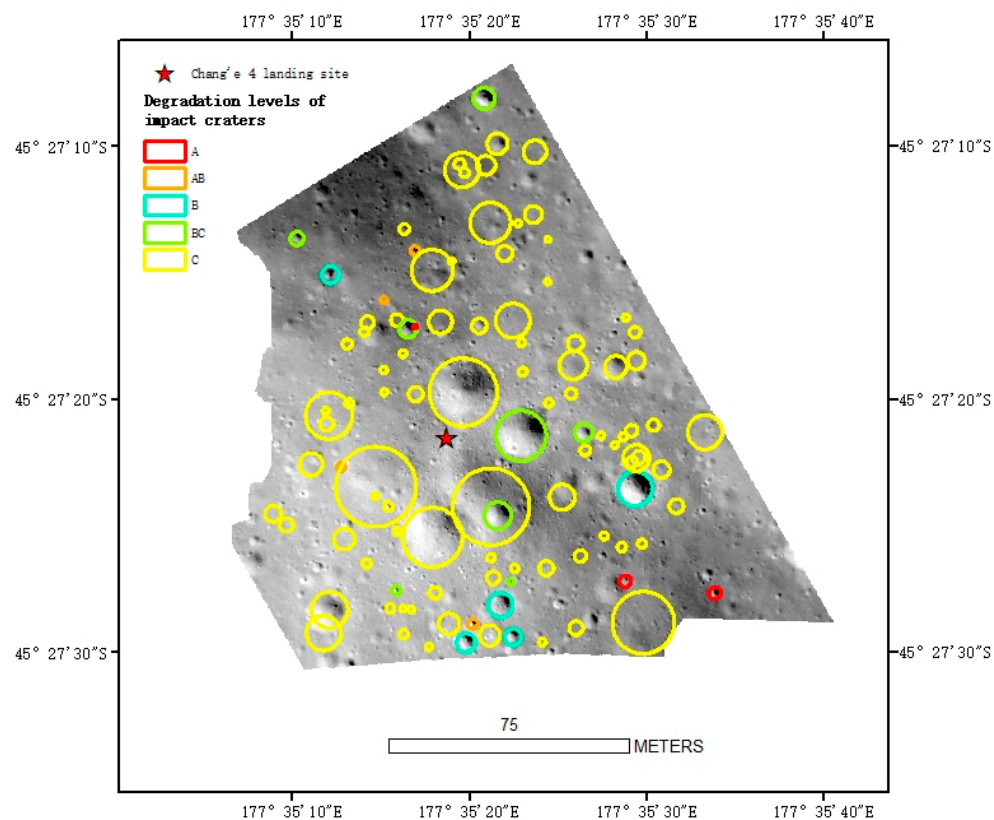

Figure 6. LCAM images and identified impact craters.

Figure 7 illustrates the image range and extraction results for the extraction of impact craters from Chang'e-4 satellite images. The total imaging area is 217.4965 km², with a strip-like shape. The imaging range encompasses the images captured by the landing camera and the panoramic camera.

The images were analysed to determine the number of impact craters visible in them. This was achieved by utilizing the panoramic camera of the rover. A total of 11,070 impact craters were counted, and the histogram of the size frequency distribution is presented in Figure 8a. Among these impact craters, the smallest diameter is 0.1005 m, the largest diameter is 6.376 m, and 70 craters have a diameter of more than 2.0 m. The number of impact craters with diameters of 0.2 m to 0.3 m was counted. The impact craters with diameters between 0.2 m and 0.3 m are the greatest in quantity at 2736, followed by those with diameters between 0.3 m and 0.4 m, with a quantity of 2434. A review of the available data indicates that more than 80% of the impact craters have a diameter between 0.2 and 0.9 m. Among these, 61.4% have a diameter between 0.2 and 0.5 metres. The impact craters extracted from the images captured with the panoramic camera are predominantly sub-metre sized, with a high degree of uniformity in size range.

The images captured by the Chang'e-4 landing camera were analysed to determine the number of impact craters present. A total of 96 impact craters were identified, and the histogram of the size frequency distribution is presented in Figure 8b. For these craters, the smallest diameter is 1.554 m, and the largest diameter is 50.870 m. A total of 64 impact craters have diameters between 2.5 m and 7.5 m, and more than 80% of the impact craters have diameters between 2.5 m and 15.0 m. It can be seen that the impact craters extracted from the images photographed with the landing camera are mainly metre-sized impact

craters. Due to the limitation of image resolution, the extracted impact craters are small in number but similar in size range.
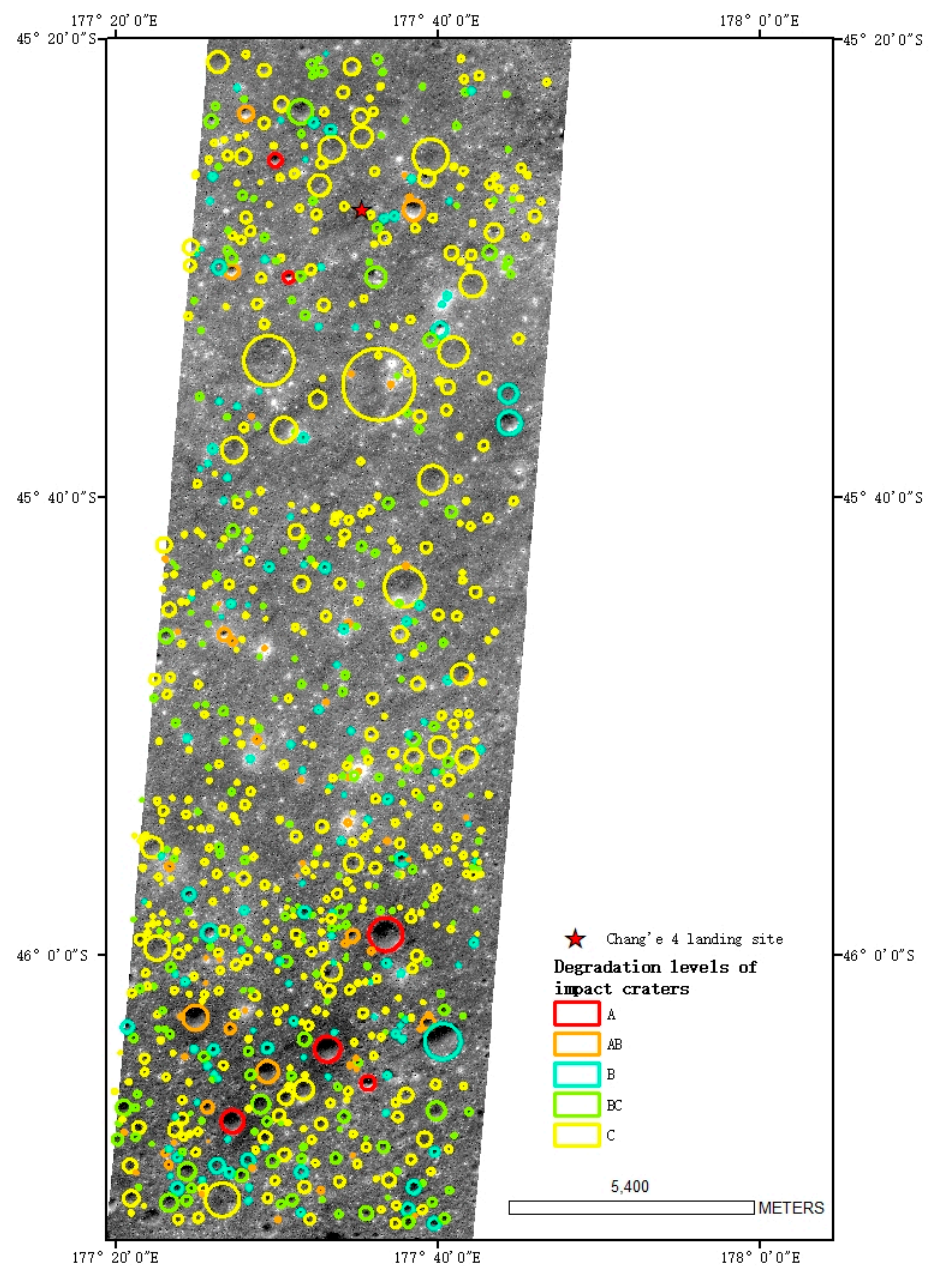

Figure 7. Satellite images (M1298916428) and identified impact craters.

We counted 923 impact craters extracted from the satellite images, and the histogram of the size frequency distribution is shown in Figure 8c. For these craters, the smallest diameter is 56.04 m, the largest diameter is 791.975 m, and more than 80% of the craters have diameters between 80.0 m and 320.0 m. The impact craters with a diameter between 120 and 160 m have the highest frequency (218), followed by those with a diameter between 80 and 120 m (152). From the data presented in the figure, it can be observed that in contrast to the smaller impact craters, those with a diameter greater than 100 m do not exhibit a similar size range. This may be influenced by the image range and resolution.
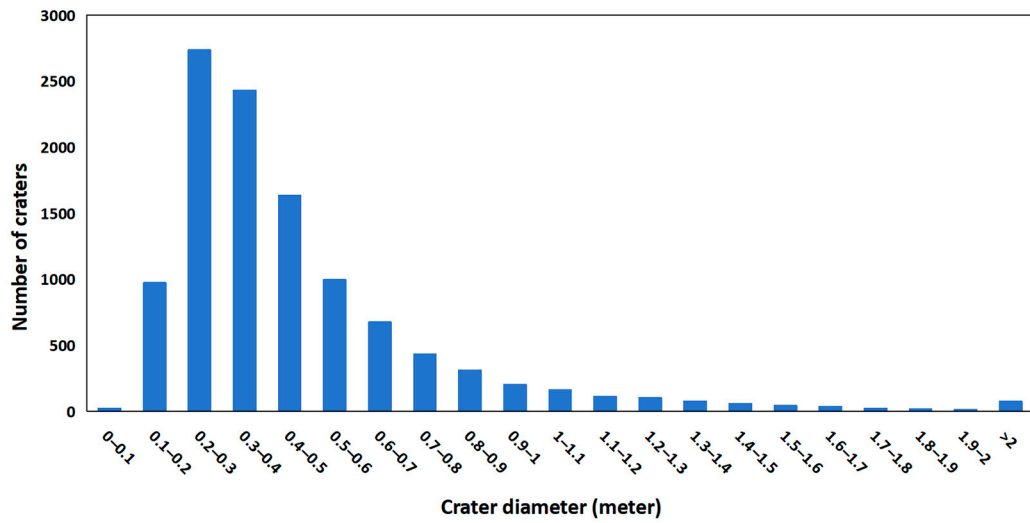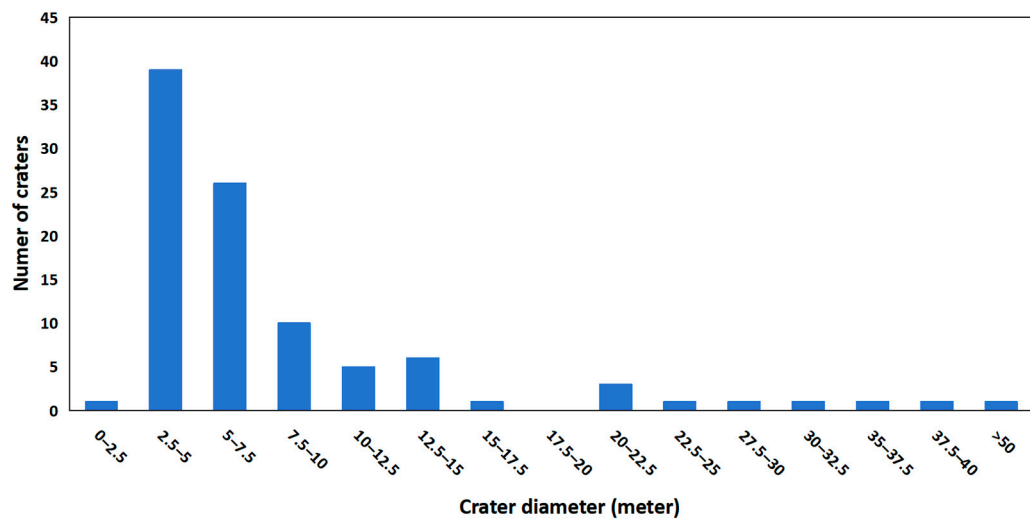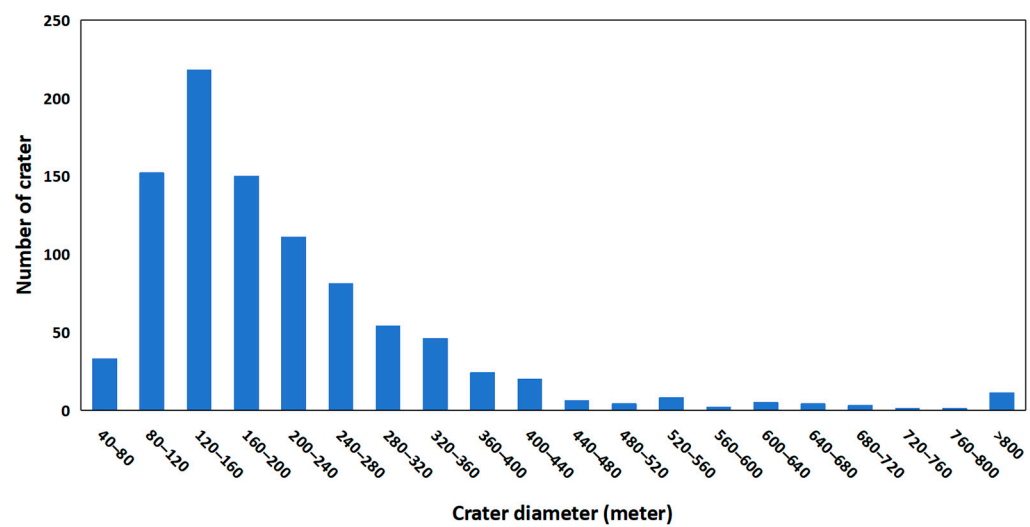
Figure 8. Histogram of frequencies versus diameters of craters. (**a**) Results of PCAM image data. (**b**) Results of LCAM image data. (**c**) Results of satellite image data.

3.2. Extraction Results of Morphological Parameters

A frequency analysis was conducted on the depth-to-diameter ratio (h/D) of impact craters extracted from images captured by the satellite, landing camera, and the panoramic camera of the rover, as illustrated in Figure 9. It can be observed that the depth-to-diameter ratios of the impact craters with varying diameters from different platforms exhibit a normal distribution. The depth-to-diameter ratios of the impact craters extracted from the images captured by the panoramic camera ranged from 0.059 to 0.261. Those extracted from the images captured by the landing camera exhibited a similar range, from 0.054 to 0.249. The depth-to-diameter ratios of the impact craters extracted from the satellite images spanned a narrower range, from 0.022 to 0.19. The mean values are 0.122, 0.115, and 0.079, respectively. In over 80% of the total impact craters photographed through platforms, the aforementioned values are 0.07–0.19, 0.04–0.16, and 0.01–0.13. Both the information in the figure and the mean values of the depth-to-diameter ratios can conclude that the average depth-to-diameter ratio of the impact craters extracted from satellite images is the smallest at 0.079, that of the landing camera is the second largest, and that of the panoramic camera is the largest at 0.122. We can conclude, based on the information in Figure 8, that 80% of the impact craters extracted from satellite images are concentrated in the range between 80.0 m and 320.0 m in diameter, 80% of those from the landing camera are concentrated in the range between 2.5 m and 15.0 m in diameter, and 80% of those from the panoramic camera are concentrated in the range between 0.2 m and 0.9 m in diameter. From this, the depth-to-diameter ratio decreases as the diameter increases, and craters of similar sizes have similar depth-to-diameter ratios, basically showing a normal distribution.

The relationship between the diameter of an impact crater and the depth-to-diameter ratio is illustrated in Figure 10. We can see that for impact craters with different diameters, the values of depth-to-diameter ratios are dispersed, and as a whole, the smallest, largest and average values of the depth-to-diameter ratios show a decreasing trend as the diameters increases, with the decreasing smallest values being mainly distributed in the vicinity of 0.05, followed by the average value, and the largest values showing the most obvious decreasing trend. For the craters with diameters between 3 m and 10 m, the depth-to-diameter ratios do not show a decreasing trend and fluctuate in the plot. This could be due to chance, because of the small amount of data in this diameter range. The incorporation of additional data within this diameter range may facilitate a more precise delineation of the evolving trend in depth-to-diameter ratios as diameters fluctuate.
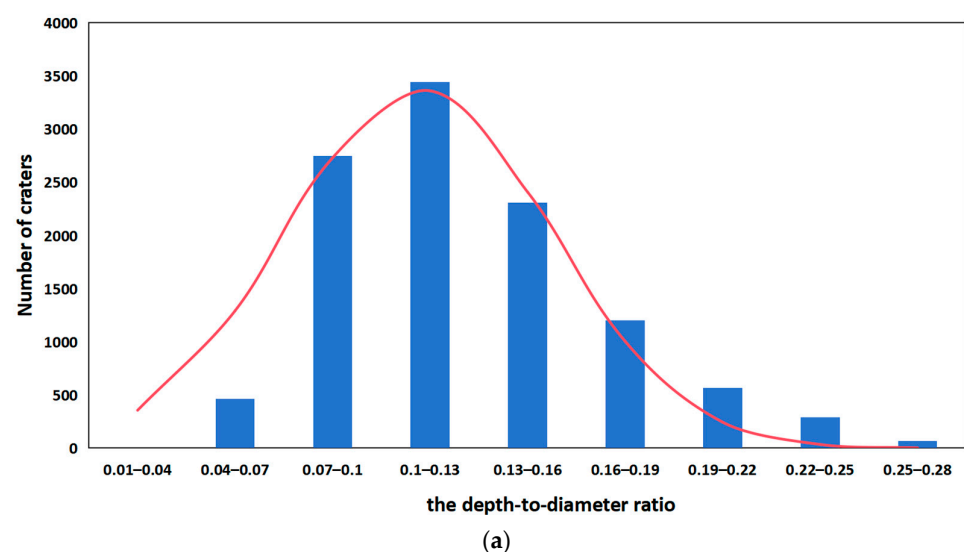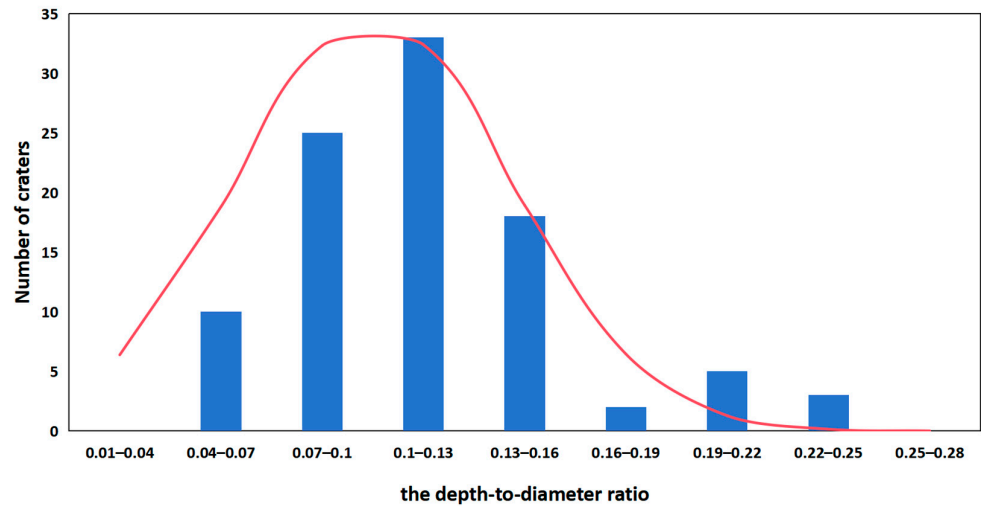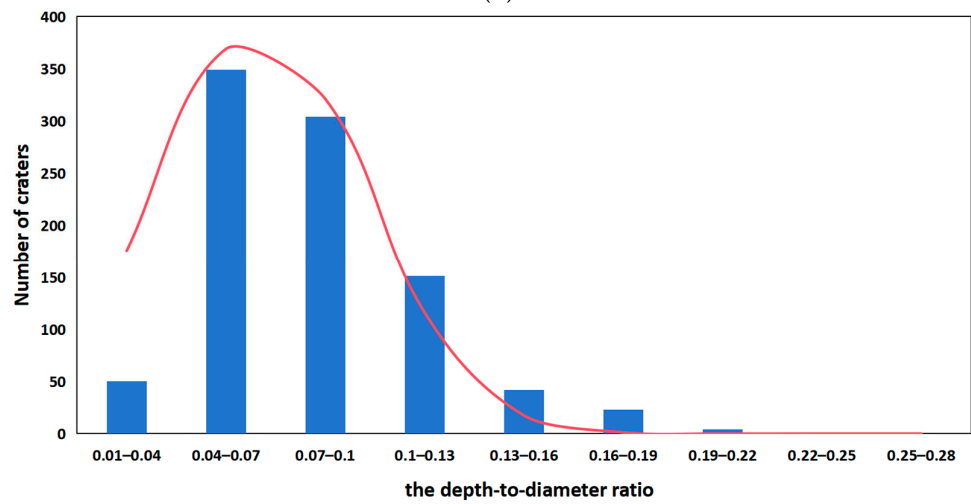

(a)

Figure 9. *Cont.*

(b)

(c)

Figure 9. Histogram of frequency versus depth-to-diameter ratio of craters. (**a**) Results of PCAM image data. (**b**) Results of LCAM image data. (**c**) Results of satellite image data. The red lines indicate the frequency curve of the data.
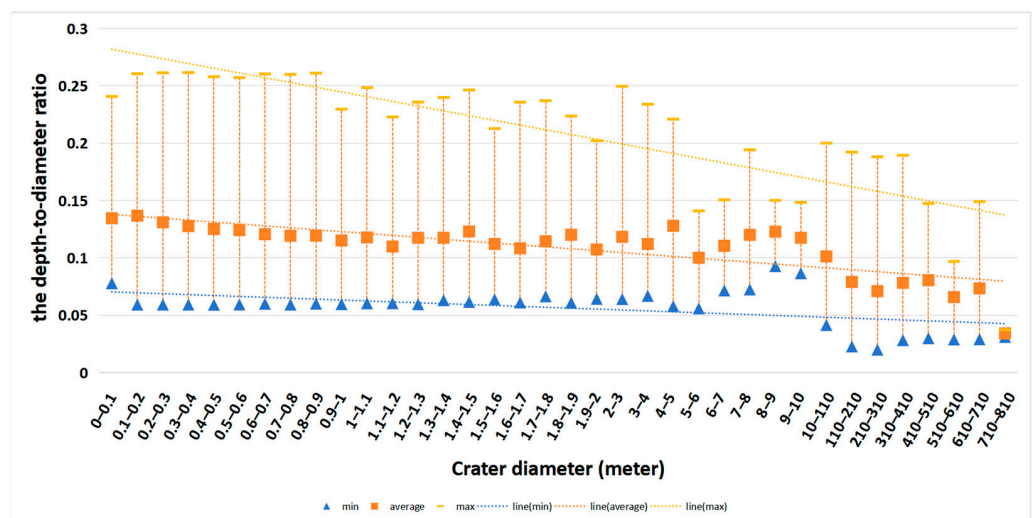

Figure 10. Trend plot of the diameter versus the depth-to-diameter ratio of craters.

3.3. Degradation Classification Results

We classified the degradation of the impact craters by voting. The PCAM images do not contain any classified A and AB impact craters. Instead, they contain 279, 2905, and 7886 craters classified as Class B, BC, and C, respectively. These craters represent 2.54%, 26.20%, and 71.26% of all craters extracted from the PCAM images. Among the impact craters extracted from the LCAM images, there are 3, 4, 5, 8, and 76 impact craters classified as Class A, AB, B, BC, and C, respectively. These represent 1.03%, 4.12%, 5.15%, 8.25%, and 81.44% of the impact craters extracted from the LCAM images. Among the impact craters extracted from the satellite image, there are 1, 46, 105, 211, and 382 craters classified as Class A, AB, B, BC, and C, respectively. These represent 0.64%, 6.75%, 14.24%, 27.09%, and 51.28% of the impact craters extracted from the satellite image. When combined with the impact craters identified by multiple platforms and their classification results, it can be concluded that the majority of impact craters are classified as Class BC and C, indicating that the majority of impact craters are severely degraded. The majority of impact craters observed through the three imaging platforms were classified as Class C, representing over 50% of the total. As the diameter of the impact craters increases, the probability of fresh impact craters shows an increasing trend. However, this trend is not significant due to the small number of impact craters in the metre-sized and 100-m-sized range that have been recorded by LCAM images and satellite images. In general, among impact craters with diameters from 0.1 m to 500 m, the smaller the size of the crater, the higher the degree of their degradation.

4. Discussion and Analysis

4.1. Comparison with Existing Results

Yang et al. analysed information on the diameter, frequency, and depth of impact craters using high-resolution images acquired by the Chang'e-4 panoramic camera on the 8th, 9th, and 11th–15th lunar days. The study focused on sub-metre to metre-sized impact craters. The results of the frequency of the diameters of 371 impact craters were analysed. Only 12 craters had diameters longer than 1 m. Furthermore, more than 50% of them had a diameter between 0.1 m and 0.3 m [24]. By measuring the depth of 63 impact craters, the researchers found that there was a clear linear relationship between depth and diameter, with most depth-to-diameter ratios falling within the range of 0.10 to 0.16. A total of 11,000 impact craters with a diameter between 0.1 m and 2.0 m were counted, with 80% exhibiting a depth-to-diameter ratio between 0.08 and 0.17. Compared with the existing results, we extracted more impact crater data with a wider range of diameters from the PCAM images, and the results obtained were more general.

4.2. Overall Morphological Parameter Analysis

We identified the impact craters in the images from each of the three platforms and analysed them separately. Figure 11 illustrates the histogram of the size frequency distribution of all the craters that we studied. It is clear that in different diameter ranges, the larger the craters are, the more the number of craters decreases.

Figure 12 illustrates the depth–diameter relationship of all of the impact craters that we studied, from which it can be seen that depth and diameter show a linear relationship, with a correlation coefficient of more than 0.8, which is higher than the result of the data from each of the three platforms. The correlation is 0.50 for data from satellite images, 0.81 for data from LCAM images, and 0.73 for data from PCAM images. The slope of the impact crater diameter versus depth, i.e., the depth–diameter ratio, ranges from 0.019 to 0.26, with most being around 0.073. It can be seen that there is a certain linear pattern between the diameter and the depth of the impact craters photographed by the different platforms, with a correlation coefficient of 0.83. An R-squared (R^2) value between 0.7 and 0.9 is generally considered to be a high fit, indicating a linear relationship between impact crater depth and diameter. Through a comprehensive study of the impact craters withdiameters between

0.1 m and 800.0 m, we can better analyse the morphological characteristics and population degradation patterns of impact craters.
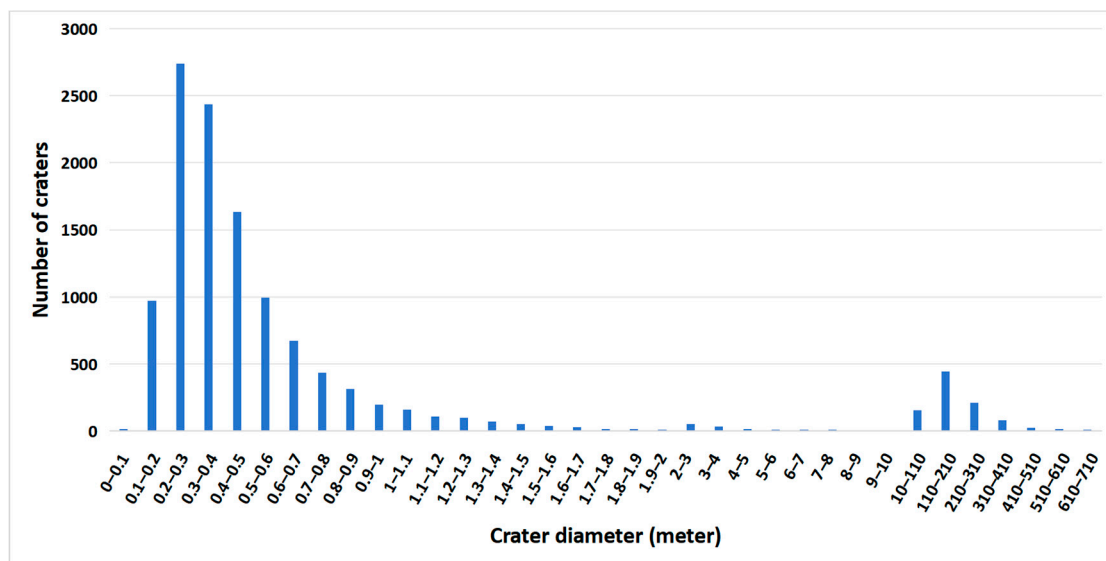

Figure 11. Histogram of frequencies versus diameters of all craters.
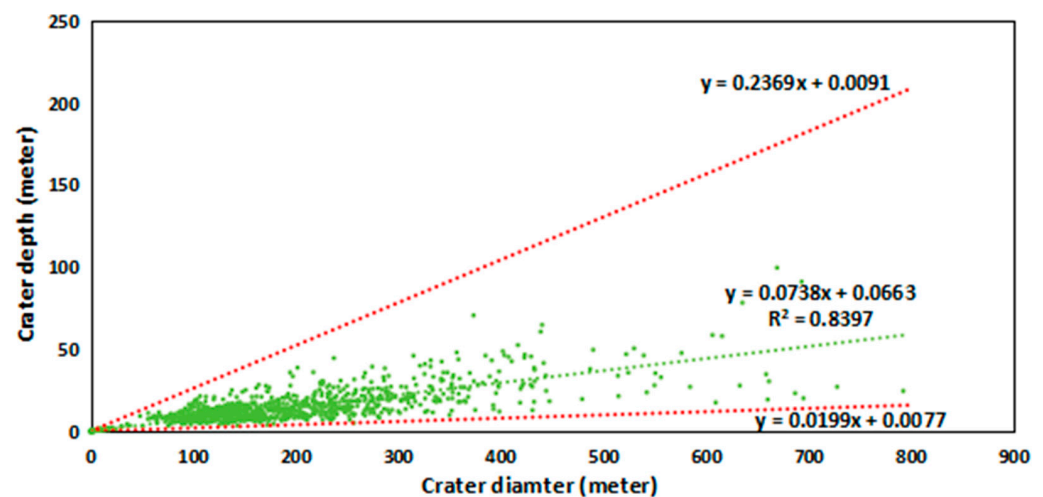

Figure 12. Depth versus diameter values of craters.

In order to discuss the trend of the depth-to-diameter ratio of impact craters with diameters between 0.1 m and 800.0 m, we analysed the image data from the satellite, landing camera, and rover together. The specific results are presented in Figure 13. The depth-to-diameter ratio of the impact craters exhibits a normal distribution, with values ranging from 0.02 to 0.26, an average of 0.122, and a variance of approximately 0.039. Over 80% of the depth-to-diameter ratios lie between 0.07 and 0.18, with 50% of the impact craters exhibiting ratios between 0.09 and 0.14. In comparison to the individual results obtained from the data from the three platforms, the results of impact craters with diameters between 0.1 m and 800.0 m are more concentrated and in accordance with the normal distribution law. A detailed examination of the morphological characteristics of the impact craters depicted in Figure 9 reveals a clear correlation between the depth-to-diameter ratio and the diameter of the craters. As the size of the impact crater increases, the depth-to-diameter ratio shows a shallowing decreasing trend. In particular, for the impact craters with diameters of 100 m and above, the depth-to-diameter ratio decreases more significantly as the size of the crater increases.
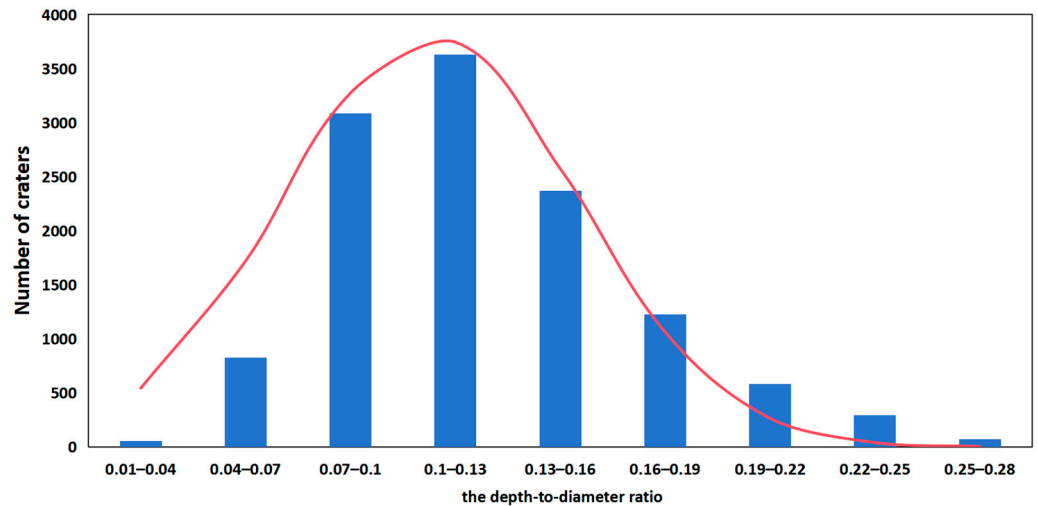
Figure 13. Histogram of frequency versus depth-to-diameter ratio of craters.

4.3. Overall Impact Crater Degradation Statistics and Analyses

To excavate the population degradation pattern of sub-metre to 100-m-sized impact craters, we analysed the data of impact craters with diameters ranging from 0.1 m to 800.0 m from the three platforms in combination. Figure 14 illustrates the degradation conditions after we classified all studied impact craters by vote. The percentages of Class A to Class C were, respectively, 0.06%, 0.55%, 3.46%, 26.13%, and 69.80%, and the corresponding numbers of the impact craters were 6, 67, 418, 3165, and 8443. It is evident that the morphology of the impact craters is challenging to discern within the study range, and the degradation is significant.
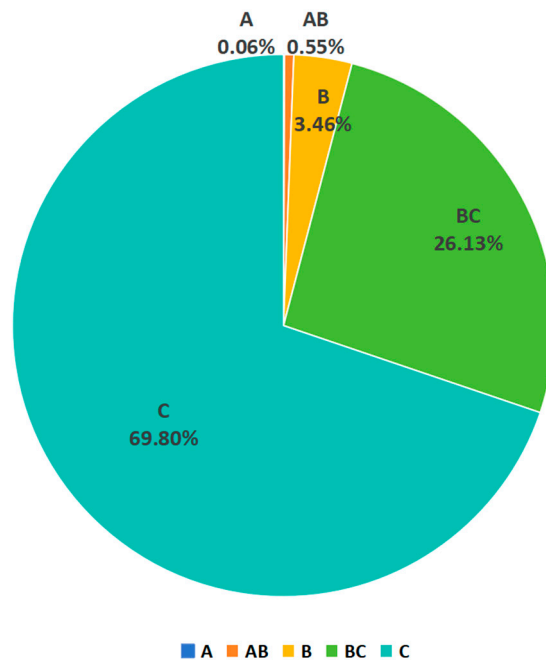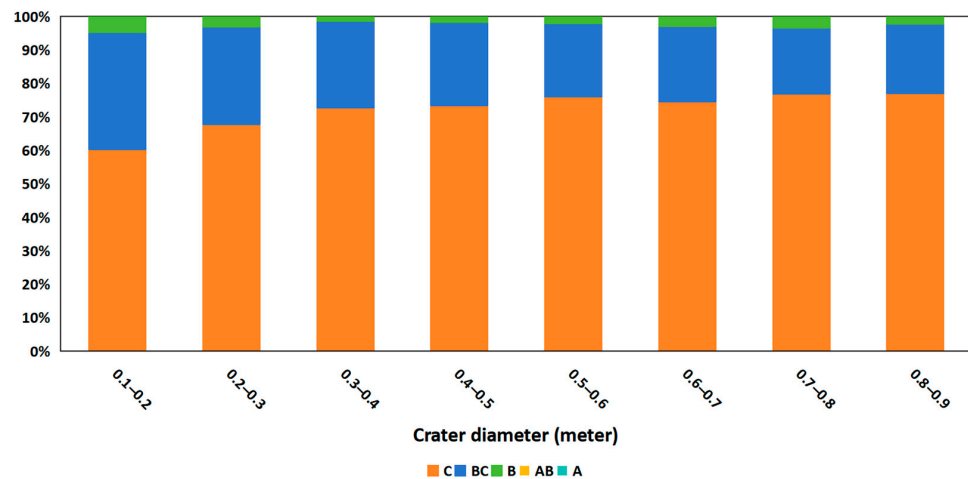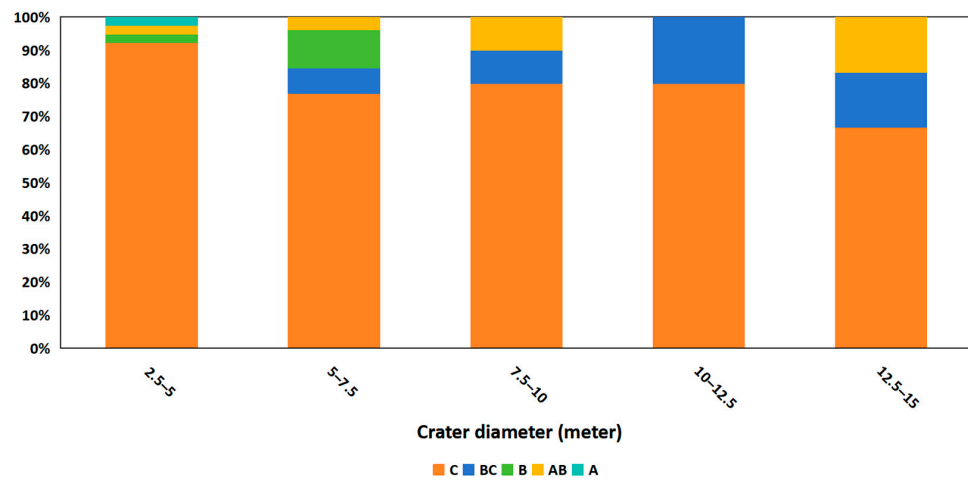

Figure 14. Crater degradation class.

The relationship between the diameter and degradation class of impact craters was presented in the form of a percentage. The percentage of the degradation classes of impact craters was analysed by taking craters with different diameter ranges (0.1–0.9 m, 2.5–15 m, and 80–320 m), which account for 80% of the craters of each platform, in order to reduce the occasional error due to the small number of craters. The results are presented in Figure 15. It can be observed that the majority of impact craters exhibit class C characteristics, regardless

of their diameter. Figure 15a demonstrates that the degree of degradation of impact craters increases as the diameter of craters between 0.1 m and 0.9 m increases. Figure 15b illustrates the percentage of degradation of impact craters with diameters of between 2.5 and 15 m. It can be seen that Class A, Class AB, and Class B occur in the impact crater population with a diameter of between 2.5 and 5 metres. At 0 m, Class AB and Class B occur in the impact crater population with diameters from 5.0 m to 7.5 m. Among the impact craters with diameters greater than 7.5 m, Class BC and Class C account for the majority of the total, indicating that the majority of craters are in a state of severe degradation. However, the number of impact craters with diameters between 2.5 and 15 m is relatively small, with only 125 craters in this category. This results in a significant deviation. The impact craters with diameters of 0.1–1 m and 80.0–320.0 m are more statistically meaningful. Under these conditions, it can be concluded that the degradation degree of impact craters increases as the size of the craters increases. Figure 15c illustrates the percentage of degradation of impact craters with diameters from 80.0 m to 320.0 m. It can be seen that Class A and Class AB in a minor degradation state account for most of the craters with diameters from 80.0 m to 120.0 m, and the percentage decreases as the diameter increases. It can also be seen that Class BC and Class C in a severe degradation state account for the least of the craters with diameters from 80.0 m to 120.0 m, and the percentage increases as the diameter increases. Furthermore, it can be observed that the degree of degradation of the craters increases with increasing diameter. In conclusion, it can be posited that the degree of degradation of an impact crater increases as the crater itself becomes larger.
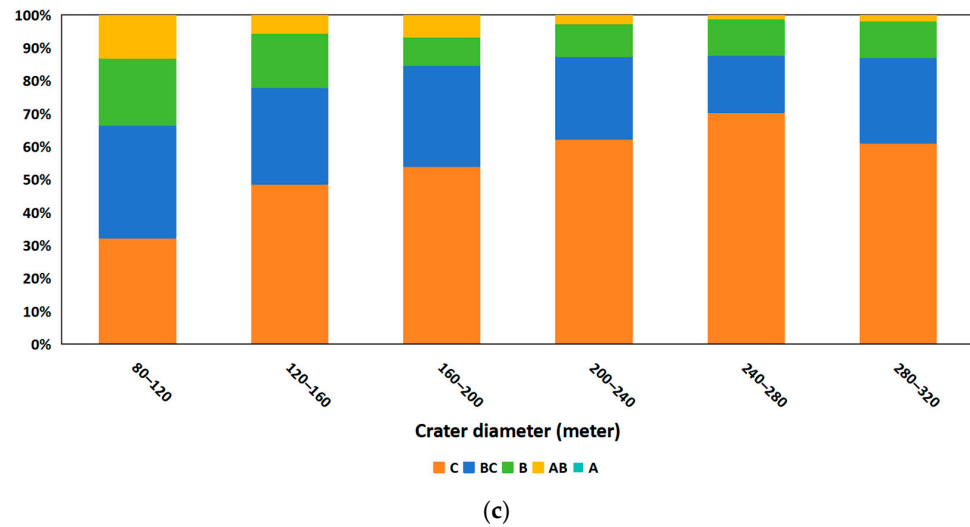

(a)

(b)

Figure 15. *Cont.*

(**c**)

Figure 15. Histogram of percentage versus diameter and degradation class of craters.

The above conclusion, which states that the degradation of impact craters becomes severe as the crater becomes larger, would suggest that there should be a large number of fresh impact craters with a diameter below 1 m or even 2 m. However, this is not the case. A detailed analysis was conducted using images captured by the panoramic camera on the rover. This analysis included the identification of specific cases, as illustrated in Figure 16. The analysis also included a summary of the reasons for the observed results: The Basilevsky and Head study mentioned a simple method for estimating the total life cycle of impact craters [32]. The method mentions that the total life cycle of small impact craters is linearly and positively correlated with the diameter of the crater. From that, we can tell that the smaller the diameter of the impact crater, the faster its degradation rate. Thus, the degradation rate of sub-metre craters is faster than that of metre and 100-m craters, so that smaller impact craters are degraded more severely.

Sub-metre-sized impact craters are generated on the lunar surface by minor impacts. Due to the limited impact energy and the absence of intense material melting processes, the size of the formed craters is limited. In comparison to large impact craters, the crater wall materials are not sufficiently solid to withstand the degradation processes that are more likely to occur. It can be seen that, although there is a high probability of new sub-metre-sized impact craters appearing on the lunar surface, the crater rims are not solid and easily degrade compared with the metre-sized impact craters. It is the case that some sub-metre-sized impact craters have a high depth-to-diameter ratio, but have a broken and incomplete lip, resulting in the judgement of moderate or severe degradation.
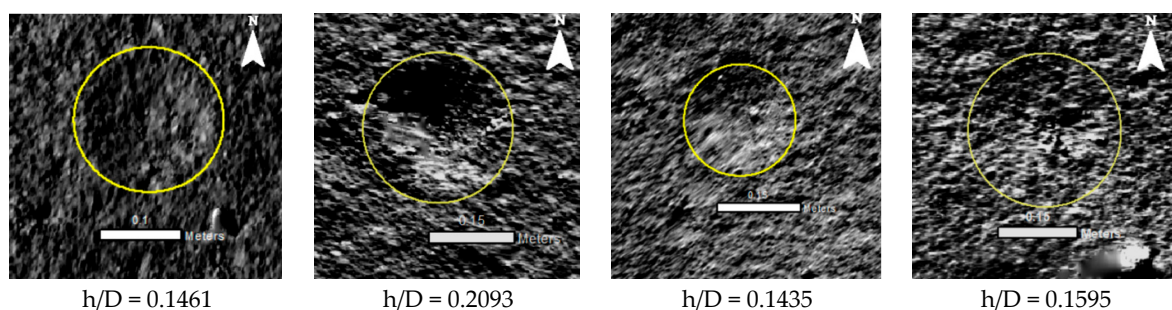

| h/D = 0.1461 | h/D = 0.2093 | h/D = 0.1435 | h/D = 0.1595 |

Figure 16. Examples of impact craters, including results of morphology and depth-to-diameter ratio in DOM images. The yellow outlined areas correspond to impact craters identified.

4.4. Saturation Analysis

As impact events continue to increase, impact crater densities eventually reach the upper limit [15,33,34], especially in the craters with a shorter diameter. When the generation rate of craters is balanced against the removal rate [34], the crater population with diameters shorter than a given diameter is considered to be in equilibrium. The methods of Gault [35] and Hartmann [36] are widely used to assess the equilibrium state of impact crater populations; both methods take some empirical impact crater density as the equilibrium level. CraterStats2 [2] software was employed to plot Hartmann equilibrium lines for impact craters in the satellite image area, the lander landing area, the area along the rover, and the three areas collectively, as illustrated in Figure 17. The points representing the impact craters in the satellite image area are located below the equilibrium curve. The impact craters in the landing area are distributed on both sides of the equilibrium curve, although the number of identified impact craters is limited by the image resolution. The points of impact craters in the area along the rover are concentrated near the equilibrium curve, with a clear inflection point at 0.2 m.
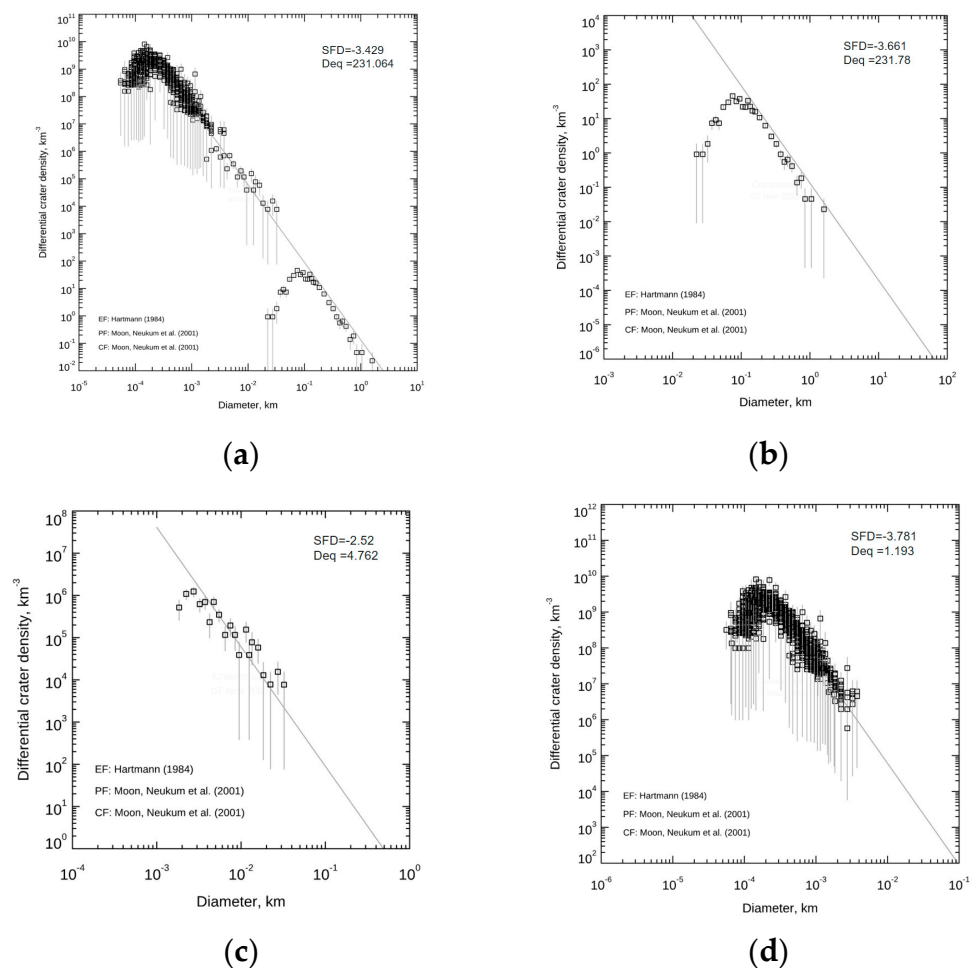

Figure 17. Craterstats2-program-calculated equilibrium lines. (**a**) The three areas as a whole. (**b**) The satellite imagery area. (**c**) The landing area. (**d**) The area along the route of the rover. EF refer to the equilibrium function of Hartmann [36]. PF and CF refer to the production function and the chronology function of Neukum et al. [4], respectively.

Due to the resolution limitations of the images captured by the rover, the images of impact craters with shorter diameters (less than 0.2 m) were not fully extracted. To ensure the completeness of the extracted results, a lower limit for the diameters of impact craters taken along the route by the rover at each station was set, as shown in Figure 18.
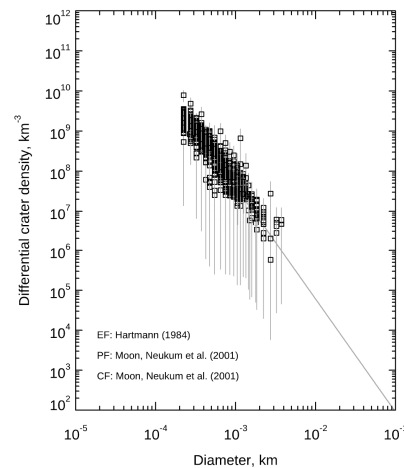
Figure 18. Craterstats2-program-calculated equilibrium lines of the area along the rover. EF refer to the equilibrium function of Hartmann [36]. PF and CF refer to the production function and the chronology function of Neukum et al. [4], respectively.

The equilibrium state of the impact crater populations obtained from each of the three platforms was evaluated, and the technique of Clauset et al. [37] was employed to fit a power law to the impact craters in each area in order to obtain the cumulative SFD slope and equilibrium onset diameter (Deq). In previous studies, impact crater populations with diameters below a given threshold were considered to be in equilibrium when the generation rate of impact craters was balanced against the removal rate. In an equilibrium state, the cumulative SFD slope of the impact crater population with diameters ranging from decimetres to hundreds of metres is −2, while the production slope is −3 [38]. For a given crater population, the diameter of the largest crater at which the population is in equilibrium is called the equilibrium onset diameter (Deq) [34]. As shown in Table 2, the cumulative SFD slope for the satellite image area is −3.661 and the equilibrium onset diameter is 231.708. The results are −2.52 and 4.762 for the landing area, and for the area along the route of the rover, they are −3.781 and 1.193, respectively. It seems that the area of statistics did not reach the equilibrium level of impact craters. Recent geological surveys show that the Von Karmen impact crater is about 3.6–3.7 Gyr (pre-tectonic) [39]. We therefore suppose that the Chang'e-4 landing zone and the area along the rover may be old and the weathering layers may be thick. Therefore, there may be a large distribution of secondary impact craters, which are more likely to be distributed widely in the area of craters with sub-metre diameters. Again, they are difficult to balance because the fresh impact craters produced on the lunar surface are mainly metre-sized or sub-metre-sized craters, which are easily degraded; their sides are not robust and they are easily buried by sputtering. Therefore, it is difficult for them to reach an equilibrium. The conclusion that the smaller the impact crater, the less easy the equilibrium is can be important for the geological background and its evolution in the Chang'e-4 landing area.

Table 2. Summary of the equilibrium states of the crater populations on the counting areas.

Counting Areas	Cumulative SFD Slopes of Crater Population in Equilibrium	D_{eq} (m)
Satellite imagery area	−3.661	231.708
Landing area	−2.52	4.762
Area along the route of the rover	−3.781	1.193
The three areas as a whole	−3.429	231.064

5. Conclusions

We focused on the study of the morphological characteristics and degradation patterns of impact craters from multiple platforms. Through the joint analysis of the image data

from the satellite (0.8 m/pixel), the landing camera (0.05 m/pixel to 0.09 m/pixel) and the panoramic camera (0.0011 m/pixel to 0.004 m/pixel), we identified 12,089 impact craters with diameters ranging from 0.1 m to 800.0 m and classified them into different degradation classes. The results of the study are shown below:

(1) The impact crater populations exhibit a higher degree of degradation, with more than 90% of the impact craters exhibiting moderate to severe degradation (Class B, BC, and C). Furthermore, the pattern of degradation observed in large impact crater populations is mirrored in the impact crater population itself, with the degradation becoming increasingly severe as the size of the craters increases.

(2) Compared with the data from the other two platforms mentioned in the paper, although the impact craters with diameters of less than 2 m in the PCAM images have higher depth-to-diameter ratios, these impact craters are more degraded because of their lower depths, their ease of burial by spatter, and the fact that their rims are not robust, so their degradation is severe. But due to the large number of impact craters extracted, fresh craters and slightly degraded craters also appear; as a whole, the degradation of the sub-metre-sized impact craters is less severe than the metre- and kilometre-sized impact craters.

(3) As fresh craters are likely sub-metre–sized (mainly below 2.0 m in diameter), their lower depths and less robust rims can be more easily buried by spatter. As a result, it is more difficult for them to reach equilibrium (their cumulative SFD is −3.781).

6. Future Research Considerations

The large number of impact craters of various diameter (centimetre to kilometre scale) on the lunar surface and the limitations of image resolution present a challenge for the identification and categorisation of secondary impact craters from the images. It is anticipated that future studies will include more accurate parameters and samples regarding impact crater extraction and identification. Alternatively, higher spectral resolution images may be available for a more comprehensive understanding of secondary impact craters.

In contrast to the single-angle study, the multi-platform analysis is capable of providing an overview of the morphological characteristics and degradation patterns of sub-metre-sized, metre-sized and even 100-m-sized impact craters. The data and results will be useful for more detailed statistical and degradation analyses of sub-metre-sized craters to kilometre-sized craters on the lunar surface, as well as for statistical analyses of impact craters on other celestial bodies in the future. Furthermore, the statistical analysis of sub-metre-sized and 100-m-sized impact craters can contribute to the study of the geological evolution of the lunar surface.

References

1. Ouyang, Z.Y.; Li, C.L.; Zou, Y.Y.; Liu, J.Z. Progress of scientific application and research of China's circumlunar exploration program. *Bull. Chin. Acad. Sci.* **2009**, *24*, 530–536. [CrossRef]
2. Michael, G.G.; Neukum, G. Planetary surface dating from crater size-frequency distribution measurements: Partial resurfacing events and statistical age uncertainty. *Earth Planet. Sci. Lett.* **2010**, *294*, 223–229. [CrossRef]
3. Ouyang, Z.Y.; Li, C.L.; Zou, Y.Y.; Liu, J.Z. The primary science results from the Chang' e-1 probe. *Chin. J. Nat.* **2010**, *32*, 249–266.
4. Neukum, G.; Lvanov, B.A.; Hartmann, W.K. Cratering Records in the Inner Solar System in Relation to the Lunar Reference System. *Space Sci. Rev.* **2001**, *96*, 55–86. [CrossRef]
5. Yue, Z.Y.; Shi, K.; Di, K.C.; Lin, Y.T.; Gou, S. Progresses and prospects of impact crater studies. *Sci. China-Earth Sci.* **2023**, *66*, 2441–2451. [CrossRef]
6. Hargitai, H.; Kereszturi, A. *Encyclopedia of Planetary Landform*; Springer: Berlin/Heidelberg, Germany, 2015. [CrossRef]
7. Kereszturi, A.; Steinmann, V. Characteristics of small young lunar impact craters focusing on current production and degradation on the Moon. *Planet. Space Sci.* **2017**, *148*, 12–27. [CrossRef]
8. Neukum, G.; Mehl, A.; Fechtig, H.; Zahringer, J. Impact phenomena of micrometeorites on lunar surface material. *Earth Planet Sci. Lett.* **1970**, *8*, 31–35. [CrossRef]
9. Jia, Y.; Zou, Y.; Xue, C.; Ping, J.; Yan, J.; Ning, Y. Scientific Objectives and Payloads of Chang'E-4 Mission. *Chin. J. Space Sci.* **2018**, *38*, 118–130. [CrossRef]
10. Craddock, R.A.; Howard, A.D. Simulated degradation of lunar impact craters and a new method for age dating farside mare deposits. *J. Geophys. Res. Planets* **2000**, *105*, 20387–20401. [CrossRef]
11. Haruyama, J.; Ohtake, M.; Matsunaga, T. Detectability of Degradation of Lunar Impact Craters by SELENE Terrain Camera. In Proceedings of the 35th Lunar and Planetary Science Conference, League City, TX, USA, 15–19 March 2004.
12. Wood, C.; Head, J.; Cintala, M. Crater degradation on Mercury and the Moon: Clues to surface evolution. In *Lunar Science Conference, 8th, Houston, TX, USA, 14–18 March 1977*; Proceedings (A78-41551 18-91); Pergamon Press, Inc.: New York, NY, USA, 1977; Volume 3.
13. Ivanov, M.; Basilevsky, A. Morphology and Size–Frequency Distribution of Kilometer-Scale Impact Craters on Callisto and Ganymede Derived from Galileo Data. *Sol. Syst. Res.* **2002**, *36*, 447–457. [CrossRef]
14. Hartmann, W.K.; Gaskell, R.W. Planetary cratering 2: Studies of saturation equilibrium. *Meteorit. Planet. Sci.* **1997**, *32*, 109–121. [CrossRef]
15. Richardson, J.E. Cratering saturation and equilibrium: A new model looks at an old problem. *Icarus* **2009**, *204*, 697–715. [CrossRef]
16. Arthur, D.; Agnieray, A.; Horvath, R.; Wood, C.; Chapman, C. The System of Lunar Craters, Quadrant I. *Commun. Lunar Planet. Lab.* **1964**, *2*, 71–78.
17. Basilevskii, A.T. On the evolution rate of small lunar craters. *Lunar Planet. Sci. Conf. Proc.* **1976**, *1*, 1005–1020.
18. Bo, Z.; Di, K.C.; Liu, Z.Q.; Yue, Z.Y.; Liu, J.; Shi, K. A catalogue of meterscale impact craters in the Chang'e-5 landing area measured from centimeter-resolution descent imagery. *Icarus* **2022**, *378*, 114943. [CrossRef]
19. Mahani, P.; Robinson, M.S.; Thompson, T.J.; Henriksen, M.R. Small lunar craters at the Apollo 16 and 17 landing sites-morphology and degradation. *Icarus* **2018**, *299*, 475–501. [CrossRef]
20. Sun, S.J.; Yue, Z.Y.; Di, K.C. Investigation of the depth and diameter relationship of subkilometer-diameter lunar craters. *Icarus* **2018**, *309*, 61–68. [CrossRef]
21. Prieur, N.C.; Rolf, T.; Wünnemann, K.; Werner, S.C. Formation of Simple Impact Craters in Layered Targets: Implications for Lunar Crater Morphology and Regolith Thickness. *J. Geophys. Res.-Planets* **2018**, *123*, 1555–1578. [CrossRef]
22. Losiak, A.; Wilhelms, D.E.; Byrne, C.J.; Thaisen, K.G.; Weider, S.Z.; Kohout, T.; O'Sullivan, K.; Kring, D.A. A new lunar crater database. In Proceedings of the 40th Lunar and Planetary Science Conference, The Woodlands, TX, USA, 23–27 March 2009.
23. Shi, K.; Yue, Z.Y.; Di, K.C.; Niu, J.Z.; Niu, S.L. Comparative Analysis of the Degradation of Impact Craters Between the Apollo 11 and Chang'e-4 Landing Areas. *Bull. Mineral. Petrol. Geochem.* **2021**, *40*, 711–719. [CrossRef]
24. Yang, M.; Yue, Z.; Di, K.; Wan, W.; Liu, J.; Shi, K. Statistical Analysis of Secondary Craters in the Chang'E-4 Landing Area Based on Panoramic Camera Data. *Bull. Mineral. Petrol. Geochem.* **2021**, *40*, 720–729.
25. Hu, T.; Yang, Z.; Kang, Z.Z.; Lin, H.Y.; Zhong, J.; Zhang, D.Y.; Cao, Y.M.; Geng, H.M. Population of Degrading Small Impact Craters in the Chang'E-4 Landing Area Using Descent and Ground Images. *Remote Sens.* **2022**, *14*, 3608. [CrossRef]
26. SELenological and ENgineering Explorer. SELENE Data Archive. Available online: https://darts.isas.jaxa.jp/planet/pdap/selene/index.html.en (accessed on 16 June 2023).
27. Ground Research and Application System of China's Lunar and Planetary Exploration Program. Chang'E 4 Panoramic Cameras Dataset. China National Space Administration. 2020. Available online: http://moon.bao.ac.cn (accessed on 19 November 2022).
28. Dai, S.; Wu, J.; Sun, H.; Zhang, B.; Yang, J.; Fang, G.; Wang, J.; Wang, H.; An, J. Chang'E-3 Lunar Rover's Scientific Payloads. *Chin. J. Space Sci.* **2014**, *34*, 332–340. [CrossRef]
29. Kneissl, T.; van Gasselt, S.; Neukum, G. CraterTools. Available online: https://www.geo.fu-berlin.de/en/geol/fachrichtungen/planet/software/index.html (accessed on 22 July 2023).
30. Xiao, M.; Hu, T.; Kang, Z.Z.; Zhao, H.F.; Liu, F. Automatic extraction of multiple morphological parameters of lunar impact craters. *Photogramm. Rec.* **2024**, *39*, 259–293. [CrossRef]

31. Wang, Y.C.; Xie, M.G.; Xiao, Z.Y.; Cui, J. The minimum confidence limit for diameters in crater counts. *Icarus* **2020**, *341*, 113645. [CrossRef]
32. Basilevsky, A.T.; Head, J.W. Age of Giordano Bruno crater as deduced from the morphology of its secondaries at the Luna 24 landing site. *Planet. Space Sci.* **2012**, *73*, 302–309. [CrossRef]
33. Melosh, H.J. *Impact Cratering: A Geologic Process*; Oxford University Press: New York, NY, USA; Clarendon Press: Oxford, UK, 1989; pp. 1–255.
34. Xiao, Z.Y.; Werner, S.C. Size-frequency distribution of crater populations in equilibrium on the Moon. *J. Geophys. Res. Planets* **2015**, *120*, 2277–2292. [CrossRef]
35. Gault, D.E. Saturation and Equilibrium Conditions for Impact Cratering on the Lunar Surface: Criteria and Implications. *Radio Sci.* **1970**, *5*, 273–291. [CrossRef]
36. Hartmann, W.K. Does crater "saturation equilibrium" occur in the solar system? *Icarus* **1984**, *60*, 56–74. [CrossRef]
37. Clauset, A.; Shalizi, C.R.; Newman, M.E.J. Power-law distributions in empirical data. *SIAM Rev.* **2009**, *51*, 661–703. Available online: https://www.jstor.org/stable/25662336 (accessed on 26 January 2024). [CrossRef]
38. Moore, H.J. Density of small craters on the lunar surface. In *United States Geological Survey Astrogeology Studies*; Annual Program Report; United States Government Printing Office: Washington, DC, USA, 1964; pp. 34–51.
39. Qiao, L.; Ling, Z.H.; Fu, X.H.; Li, B. Geological characterization of the Chang'e-4 landing area on the lunar farside. *Icarus* **2019**, *333*, 37–51. [CrossRef]